inorganics

Article

Synthesis, Crystal Structures and Thermal Properties of Ammine Barium Borohydrides

Jakob B. Grinderslev, Mads B. Amdisen and Torben R. Jensen *

Interdisciplinary Nanoscience Center (iNANO) and Department of Chemistry, Aarhus University, Langelandsgade 140, DK-8000 Aarhus C, Denmark; Jakobg@inano.au.dk (J.B.G.); mba@inano.au.dk (M.B.A.)
* Correspondence: trj@chem.au.dk

Received: 1 September 2020; Accepted: 6 October 2020; Published: 10 October 2020

Abstract: Ammine metal borohydrides show large compositional and structural diversity, and have been proposed as candidates for solid-state ammonia and hydrogen storage as well as fast cationic conductors. Here, we report the synthesis method of ammine barium borohydrides, $Ba(BH_4)_2{\cdot}xNH_3$ (x = 1, 2). The two new compounds were investigated with time-resolved temperature-varied in situ synchrotron radiation powder X-ray diffraction, thermal analysis, infrared spectroscopy and photographic analysis. The compound $Ba(BH_4)_2{\cdot}2NH_3$ crystallizes in an orthorhombic unit cell with space group symmetry $Pnc2$, and is isostructural to $Sr(BH_4)_2{\cdot}2NH_3$, forming octahedral $[Ba(NH_3)_2(BH_4)_4]$ complexes, which are connected into a two-dimensional layered structure, where the layers are interconnected by dihydrogen bonds, $N\text{–}H^{\delta+}\cdots{}^{-\delta}H\text{–}B$. A new structure type is observed for $Ba(BH_4)_2{\cdot}NH_3$, which crystallizes in an orthorhombic unit cell with space group symmetry $P2_12_12_1$, forming a three-dimensional framework structure of $[Ba(NH_3)(BH_4)_6]$ complexes. The structure is built from distorted hexagonal chains, where NH_3 groups form dihydrogen bonds to the nearby BH_4^--groups within the chain. $Ba(BH_4)_2{\cdot}2NH_3$ is unstable at room temperature and releases NH_3 in two subsequent endothermic reactions with maxima at 49 and 117 °C, eventually reforming $Ba(BH_4)_2$. We demonstrate that the thermal stability and composition of the gas release for the ammine alkaline earth metal borohydrides can be correlated to the charge density of the metal cation, but are also influenced by other effects.

Keywords: complex metal hydrides; ammine metal borohydrides; crystal structures

1. Introduction

Metal borohydrides have been intensively investigated due to their incredible diversity regarding compositions and structures. Metal borohydrides often exhibit high hydrogen densities and have thus been investigated as potential solid-state hydrogen storage materials [1–5]. However, in recent years, a number of other interesting properties have also been discovered, including magnetism [6–8], luminescence [9,10], semiconductivity [10] and high ionic conductivity, where the latter has received significant attention for the potential use as solid-state electrolytes, initiated by the investigations on the high-temperature polymorph of $LiBH_4$ [11–15].

Recently, derivatives of metal borohydrides have attracted much attention by further expanding the structural diversity and providing a range of new compositions and new varieties of materials. Metal borohydrides readily react with ammonia to form ammine metal borohydrides, which often exhibit high gravimetric and volumetric NH_3 and H_2 content, relevant for solid-state ammonia and hydrogen storage [16,17]. Ammine metal borohydrides have received particular interest due to favorable dihydrogen interactions, $N\text{–}H^{\delta+}\cdots{}^{-\delta}H\text{–}B$, in the solid state. These dihydrogen interactions may facilitate hydrogen release at low temperatures in an exothermic reaction [18–21]. Moreover, it has recently been shown that these interactions can facilitate high ionic conductivity, as observed in $LiBH_4{\cdot}xNH_3$ (x = ½, 1) and $Mg(BH_4)_2{\cdot}xNH_3$ (x = 1, 2, 3, 6), where the flexible BH_4^- coordination and the dense network of dihydrogen bonds allow for NH_3 to be exchanged between framework and migrating cations, assisting ion migration [22,23]. Composites with the composition $Mg(BH_4)_2{\cdot}xNH_3$ ($1 < x < 2$) form eutectic melts, which can be stabilized by MgO nanoparticles to form a solid-state electrolyte, exhibiting more than three orders of magnitude higher ionic conductivity than x = 1 and 2 [24].

In general, ammine metal borohydrides are formed in an exothermic reaction between a metal borohydride and gaseous ammonia. Previous studies reveal that only $LiBH_4$ reacts with ammonia amongst the alkali metal borohydrides [1]. In contrast, the alkaline earth metal borohydrides $M(BH_4)_2$ (M = Mg^{2+}, Ca^{2+}, Sr^{2+}) readily react with ammonia, forming a hexaammine for M = Mg^{2+} and Ca^{2+}, and a tetraammine for M = Sr^{2+}, with a decreasing thermal stability down the group [19,25]. The most extensive series of ammine metal borohydrides are observed for $Y(BH_4)_3{\cdot}xNH_3$ (x = 1, 2, 3, 5, 6, 7), where the isostructural compounds with RE = Gd^{3+} and Dy^{3+} were also reported for x = 3, 5, 6 and 7 [18]. Note that the structure of $RE(BH_4)_3{\cdot}5NH_3$ was recently revised, while the composition and structure of $RE(BH_4)_3{\cdot}3NH_3$, previously reported as $RE(BH_4)_3{\cdot}4NH_3$, were also revised [26]. The structures of the early rare earths $RE(BH_4)_3{\cdot}xNH_3$ (RE = La, Ce) are isostructural to the Y-analogs for x = 5 and 3, while new structures were reported for x = 6 and 4.

There are only a few reports on transition metal borohydrides (d-metals), due to the low thermal stability. However, for the compounds where the metals have the electron configuration d^0, d^5 or d^{10}, i.e., M = Mn^{2+}, Zn^{2+}, Y^{3+}, Zr^{4+}, Cd^{2+}, a higher thermal stability is observed, and the compounds are stable at ambient conditions [27–31]. Some of the unstable transition metal borohydrides can be stabilized in solution, e.g., M = Cr^{2+}, Fe^{2+} and Co^{2+} are stable in dimethyl sulfide at T = −30 °C [32]. The corresponding ammines are reported for the stable transition metal borohydrides, including $Mn(BH_4)_2{\cdot}xNH_3$ (x = 2, 3, 6), $Zn(BH_4)_2{\cdot}xNH_3$ (x = 2, 4), $Y(BH_4)_3{\cdot}xNH_3$ (x = 1, 2, 3, 5, 6, 7) and $Zr(BH_4)_4{\cdot}8NH_3$ [1,18,33,34]. Interestingly, it has been shown that the unstable metal borohydrides can be stabilized by the formation of ammine transition metal borohydrides, as demonstrated for $[Fe(NH_3)_6](BH_4)_2$ and $[Co(NH_3)_6](BH_4)_2$, which are precipitated from solution [32]. Alternatively, the ammine-stabilized metal borohydrides can be formed by ball milling of the ammine metal chloride and $LiBH_4$, as shown for $M(BH_4)_3{\cdot}5NH_3$ (M = Ti^{3+}, V^{3+}) and $Ti(BH_4)_3{\cdot}3NH_3$ [35,36]. Theoretical calculations have revealed that the metal borohydrides are always thermodynamically destabilized by ammonia, but in the case of the unstable metal borohydrides with a high Pauling electronegativity of the metal ($\chi_P \geq 1.6$), the compounds are kinetically stabilized, as ammonia protects the metal from reduction and thereby alters the decomposition pathway and suppresses the release of B_2H_6 [37].

In the present investigation, we extend the family of ammine metal borohydrides to include $Ba(BH_4)_2$, thereby completing the series of the alkaline earths (excluding the toxic $Be(BH_4)_2$ [38]), in order to establish structural, chemical and physical relationships for the series of ammine alkaline earth metal borohydrides. The new compounds have been investigated with time-resolved temperature-varied in situ synchrotron radiation powder X-ray diffraction (SR-PXD), thermal analysis and Fourier transform infrared spectroscopy (FT-IR).

2. Results and Discussion

2.1. Synthesis and Initial Phase Analysis

The synthesized samples (Table 1) are denoted **s1** and **s2** and were initially characterized by PXD and FT-IR. $Ba(BH_4)_2$ (sample **s1**) was synthesized from BaH_2 and $S(CH_3)_2{\cdot}BH_3$ in a solvent-mediated reaction. Powder X-ray diffraction (PXD) of sample **s1** shows Bragg reflections from $Ba(BH_4)_2$ (82.5 wt %) and unreacted BaH_2 (17.5 wt %). Subsequently, sample **s1** was reacted with ammonia gas at T = −10 °C to form sample **s2**, and PXD revealed that $Ba(BH_4)_2$ had reacted with ammonia according to Equation (1), and Bragg reflections from two new compounds were detected, $Ba(BH_4)_2{\cdot}xNH_3$ (x = 1, 2). No clear expansion or color change of the sample was observed during the solid–gas reaction. The new compound formed in sample **s2**, $Ba(BH_4)_2{\cdot}2NH_3$, is unstable at room temperature, hence the reaction mixture was kept at $T = -10$ °C during synthesis to avoid decomposition. Furthermore, the reaction between $Ba(BH_4)_2$ and NH_3 was expected to be exothermic, as also observed for other ammine metal borohydrides [18,19,25,26]. $Ba(BH_4)_2 \cdot 2NH_3$ gradually releases NH_3 and forms $Ba(BH_4)_2 \cdot NH_3$ if a vacuum is applied for a longer period at −10 °C (>10 min).

$$Ba(BH_4)_{2(s)} + 2\,NH_{3(g)} \rightarrow Ba(BH_4)_2 \cdot 2NH_{3(s)} \quad (1)$$

Table 1. Sample overview.

Sample	Reactants	Products after Synthesis
s1	BaH_2 + DMS-BH_3	$Ba(BH_4)_2 + BaH_2$
s2	$Ba(BH_4)_2 + NH_3$ (+ BaH_2)	$Ba(BH_4)_2 \cdot 2NH_3 + Ba(BH_4)_2 \cdot NH_3 + BaH_2$

FT-IR data reveal absorbance modes at 500–700 cm^{-1} in sample **s1**, which are attributed to the unreacted BaH_2, see Figure 1. The remaining absorptions observed for **s1** are in agreement with the FT-IR spectra reported for $Ba(BH_4)_2$, i.e., B–H stretch modes at 2390, 2300 and 2200 cm^{-1} and B–H bend modes at 1250, 1130 and 1090 cm^{-1} [39,40]. FT-IR data of **s2** reveal new absorption modes at 3380 and 3290 cm^{-1} and at 1550 cm^{-1}, which are assigned to N–H stretch and bend modes, respectively. The absorption modes at 2390, 2240 and 2200 cm^{-1} and at 1270, 1110 and 1080 cm^{-1} resemble those of $Ba(BH_4)_2$, but the peak maxima are slightly shifted. The FT-IR spectra of **s2** show similarities to what is reported for $Sr(BH_4)_2 \cdot 2NH_3$, suggesting that the structures are similar [25].

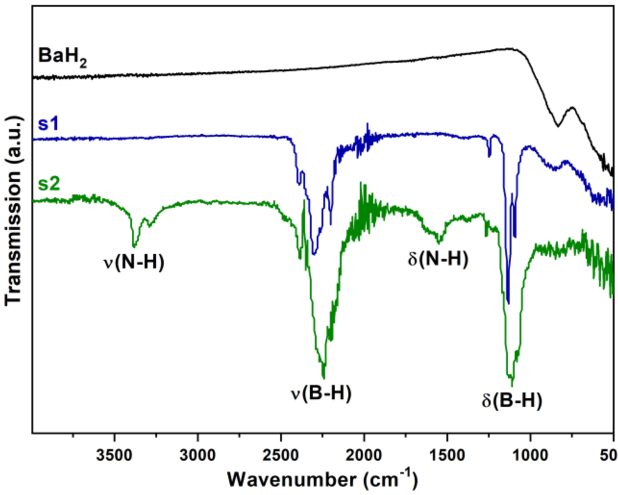

Figure 1. FT-IR spectra of BaH_2, **s1** ($Ba(BH_4)_2$) and **s2** ($Ba(BH_4)_2 \cdot 2NH_3$).

2.2. Crystal Structures

Two new compounds, $Ba(BH_4)_2 \cdot 2NH_3$ and $Ba(BH_4)_2 \cdot NH_3$, were synthesized and structurally characterized in this work, see Table 2 and CIF files in Supplementary Materials. Rietveld refinements are provided in Figure 2. The unit cell volume per formula unit as a function of the number of ammonia molecules for $Ba(BH_4)_2 \cdot xNH_3$ is shown in Figure 3, where NH_3 has an effective volume of ~40.8 Å^3 per NH_3. This value is higher as compared to that of solid ammonia, i.e., $V(NH_3) = 33.9$ Å^3 per ammonia at $T = -102$ °C [41]. In comparison, NH_3 has an effective volume of 33.1 Å^3 in $Mg(BH_4)_2 \cdot xNH_3$ (x = 1, 2, 3, 6), 35.6 Å^3 in $Ca(BH_4)_2 \cdot xNH_3$ (x = 1, 2, 4, 6), and 39.5 Å^3 in $Sr(BH_4)_2 \cdot xNH_3$ (x = 1, 2, 4) [25,33]. This demonstrates that NH_3 is packed less densely in $Ba(BH_4)_2 \cdot xNH_3$.

Table 2. Crystallographic data extracted by Rietveld refinement.

	$Ba(BH_4)_2{\cdot}2NH_3$	$Ba(BH_4)_2{\cdot}NH_3$
Crystal system	Orthorhombic	Orthorhombic
Space group	*Pnc*2	$P2_12_12_1$
T (°C) *	−25	95
a (Å)	6.7784(2)	5.08626(8)
b (Å)	6.7175(2)	9.3761(2)
c (Å)	8.6991(3)	12.9632(2)
V (Å^3)	396.10(2)	618.20(2)
Z	2	4
V/*Z* (Å^3)	198.1	154.6
M (g/mol)	201.08	184.05
ρ (g/mL)	1.686	1.977

* Data collection temperature.

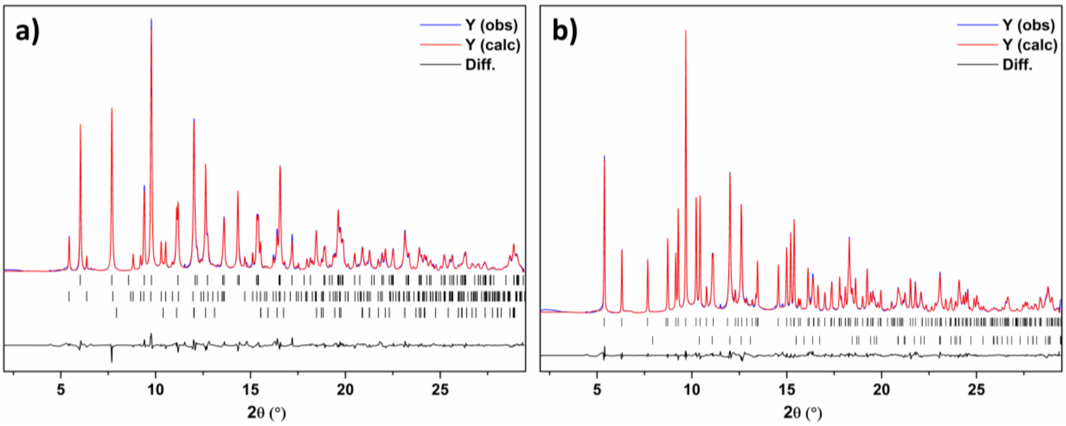

Figure 2. Rietveld refinements of synchrotron radiation powder X-ray diffraction (SR-PXD) data measured with λ = 0.7129 Å, showing experimental (blue line) and calculated (red line) PXD patterns, and a difference plot below (black line). (**a**) $Ba(BH_4)_2{\cdot}2NH_3$ is measured at *T* = −25 °C. Tick marks: $Ba(BH_4)_2{\cdot}2NH_3$ (61 wt %), $Ba(BH_4)_2{\cdot}NH_3$ (17 wt %), BaH_2 (22 wt %). Final discrepancy factors: $R_p = 3.73\%$, $R_{wp} = 4.94\%$ (not corrected for background), $R_p = 7.00\%$, $R_{wp} = 8.14\%$ (conventional Rietveld R-factors), $R_{Bragg}(Ba(BH_4)_2{\cdot}2NH_3) = 2.03\%$, $R_{Bragg}(Ba(BH_4)_2{\cdot}NH_3) = 5.45\%$, $R_{Bragg}(BaH_2) = 2.64\%$ and global $\chi^2 = 2280$. (**b**) $Ba(BH_4)_2{\cdot}NH_3$ is measured at *T* = 95 °C. Tick marks: $Ba(BH_4)_2{\cdot}NH_3$ (76 wt %), BaH_2 (24 wt %). Final discrepancy factors: $R_p = 3.04\%$, $R_{wp} = 4.20\%$ (not corrected for background), $R_p = 6.75\%$, $R_{wp} = 7.80\%$ (conventional Rietveld R-factors), $R_{Bragg}(Ba(BH_4)_2{\cdot}NH_3) = 3.04\%$, $R_{Bragg}(BaH_2) = 2.62\%$, and global $\chi^2 = 1530$.

The compound $Ba(BH_4)_2{\cdot}2NH_3$ crystallizes in an orthorhombic unit cell with space group symmetry *Pnc*2, and unit cell parameters *a* = 6.7784(2), *b* = 6.7175(2) and *c* = 8.6991(3) Å. It is isostructural to the reported structure of $Sr(BH_4)_2{\cdot}2NH_3$, despite the significant difference in size, $r(Ba^{2+}) = 1.35$ Å and $r(Sr^{2+}) = 1.18$ Å [25,42]. One unique Ba^{2+} position is coordinated by two NH_3 molecules and four bridging BH_4^- groups in an octahedral geometry, forming 2D layers in the *bc* plane, which are stacked in the sequence *AAA* along the *a*-axis, see Figure 4a. The layers are interconnected by dihydrogen bonds, $N\text{–}H^{\delta+}\cdots{}^{-\delta}H\text{–}B$, with the shortest B–N distance of 3.78 Å. Assuming that the BH_4 orientations are similar to the Sr analogue [25], the BH_4^- groups coordinate to one Ba^{2+} through the face of the tetrahedron (κ^3) and one through the edge of the tetrahedron (κ^2), thus Ba^{2+} has a coordination number of 12, see Figure 4b. This is supported by the shorter Ba–B distance of 2.86 Å for the κ^3-coordinating BH_4^-, while a Ba–B distance of 3.26 Å is observed for the κ^2-coordinating BH_4^-. The Ba–N bond distances are 2.85 Å. In comparison, the Sr–B and Sr–N distances in $Sr(BH_4)_2{\cdot}2NH_3$ are 2.86 to 3.10 Å and 2.71 Å, respectively. Thus, longer distances are observed for $Ba(BH_4)_2{\cdot}2NH_3$, as expected from the larger ionic radius of Ba^{2+}.

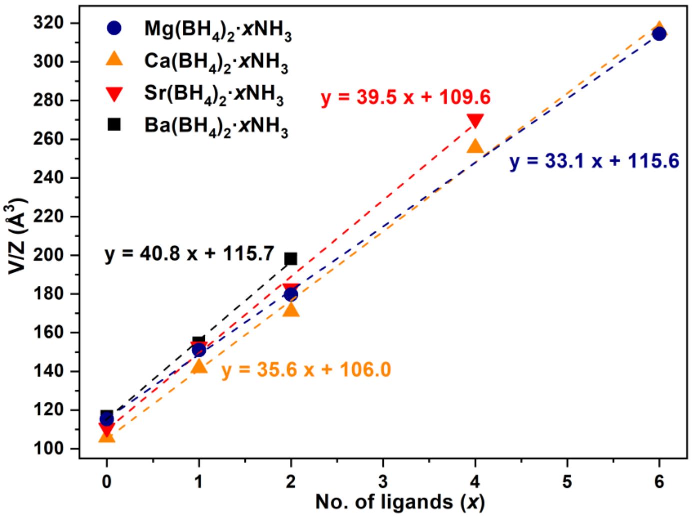

Figure 3. Volume per formula unit (V/Z) as a function of ammonia content in $Mg(BH_4)_2 \cdot xNH_3$ ($x = 1, 2, 3, 6$) (blue circles), $Ca(BH_4)_2 \cdot xNH_3$ ($x = 1, 2, 4, 6$) (orange triangles), $Sr(BH_4)_2 \cdot xNH_3$ ($x = 1, 2, 4$) (red inverted triangles) and $Ba(BH_4)_2 \cdot xNH_3$ ($x = 0, 1, 2$) (black squares).

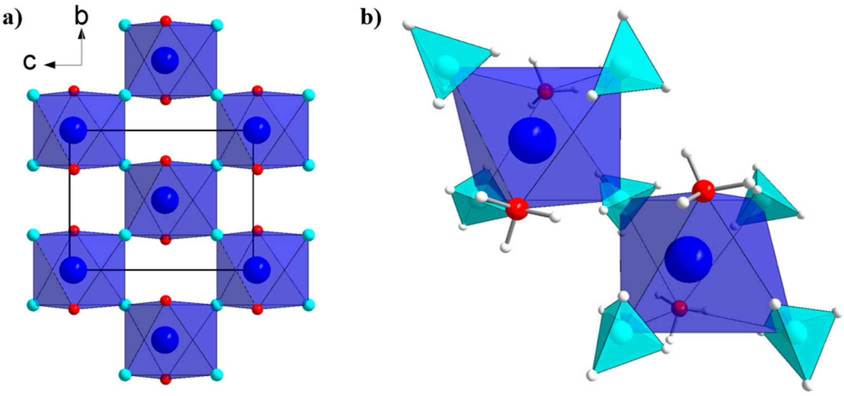

Figure 4. (**a**) Crystal structure of $Ba(BH_4)_2 \cdot 2NH_3$ (space group *Pnc*2), forming layers in the *bc* plane. Hydrogen is omitted for clarity. (**b**) Local coordination geometry of Ba^{2+} with BH_4^- and NH_3 groups in an octahedral geometry. Color scheme: Ba (blue), B (turquoise), N (red), H (white).

$Ba(BH_4)_2 \cdot NH_3$ crystallizes in an orthorhombic unit cell with space group symmetry $P2_12_12_1$ and unit cell parameters $a = 5.08626(8)$, $b = 9.3761(2)$ and $c = 12.9632(2)$ Å, see Figure 5a. The structure is a new structure type, and thus different from the analogous $Sr(BH_4)_2 \cdot NH_3$. One unique Ba^{2+} position is coordinated by one NH_3 molecule and six bridging BH_4^- groups in a square-face monocapped trigonal prismatic geometry, see Figure 5b. Each prism is connected to eight other prisms: four through the edges by sharing two BH_4^- groups and four through the vertices via one BH_4^- group. The structure may be described as interconnected distorted hexagonal six-fold chains in the *bc* plane, which run along the *a*-axis. Within the chains, NH_3 groups are pointing out, forming dihydrogen bonds to the nearby BH_4^- groups, with the shortest B–N distance of 3.05 Å. Each edge of the six-fold chain is shared with the adjacent six-fold chain, forming three-dimensional networks. The six BH_4^- each bridge three Ba^{2+} with Ba–B distances in the range 3.07 to 3.48 Å, comparable to the κ^2-coordinating BH_4^- in $Ba(BH_4)_2 \cdot 2NH_3$, and a similar Ba–N distance of 2.82 Å. These distances are slightly longer than the Sr–B distances in the range 2.86 to 3.16 Å and Sr–N distance of 2.69 Å reported for the analogous $Sr(BH_4)_2 \cdot NH_3$ [25]. The H positions are not adequately determined from PXD, thus the orientation of the BH_4^- and the coordination number of Ba^{2+} are not determined. In contrast to the three-dimensional network structure of $Ba(BH_4)_2 \cdot NH_3$, the analogous $Sr(BH_4)_2 \cdot NH_3$ consists of octahedrally coordinated Sr^{2+}, where the shared octahedra form double layers in the *ab* plane. Thus, it is likely the larger size of Ba^{2+} which makes it possible to accommodate the larger coordination sphere and thereby a different structure type. The structure of $Ca(BH_4)_2 \cdot NH_3$ also forms a three-dimensional network, consisting of interconnected $[Ca(NH_3)(BH_4)_5]$ octahedra, which form rectangular-shaped chains in the *ab* plane, hence the chain geometry and the cation coordination sphere are different as compared to $Ba(BH_4)_2 \cdot NH_3$ [43].

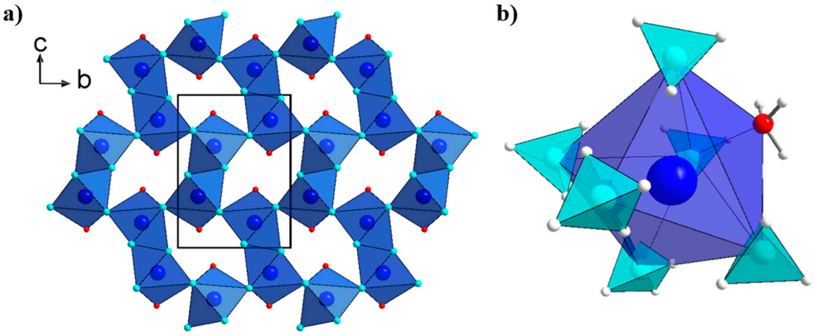

Figure 5. (**a**) Crystal structure of $Ba(BH_4)_2 \cdot NH_3$ (space group $P2_12_12_1$). Hydrogen is omitted for clarity. (**b**) Local coordination geometry of Ba^{2+} with BH_4^- and NH_3 in a square-face monocapped trigonal prismatic geometry. Color scheme: Ba (blue), B (turquoise), N (red), H (white).

2.3. In Situ Synchrotron Powder X-ray Diffraction

In situ SR-PXD experiments were conducted for sample **s2** from −30 to 225 °C ($\Delta T/\Delta t$ = 5 °C/min, p(Ar) = 1 bar), see Figure 6. The in situ SR-PXD data measured at −30 °C show Bragg reflections corresponding to $Ba(BH_4)_2 \cdot 2NH_3$ (61 wt %), $Ba(BH_4)_2 \cdot NH_3$ (17 wt %) and BaH_2 (22 wt %), see Figure 2a. The Bragg reflections corresponding to $Ba(BH_4)_2 \cdot 2NH_3$ are constant in intensity upon heating until 50 °C and disappear at 55 °C. Simultaneously, the intensity of the Bragg reflections corresponding to $Ba(BH_4)_2 \cdot NH_3$ increases, but disappears upon heating to 160 °C. At T > 160 °C, Bragg reflections corresponding to $Ba(BH_4)_2$ are observed. The Bragg reflections from BaH_2 are observed throughout the experiment, and only shift slightly due to thermal expansion. The release of ammonia from $Ba(BH_4)_2 \cdot 2NH_3$ according to in situ SR-PXD can be described according to Equation (2).

$$Ba(BH_4)_2 \cdot 2NH_{3(s)} \rightarrow Ba(BH_4)_2 \cdot NH_{3(s)} + NH_{3(g)} \rightarrow Ba(BH_4)_{2(s)} + 2NH_{3(g)} \quad (2)$$

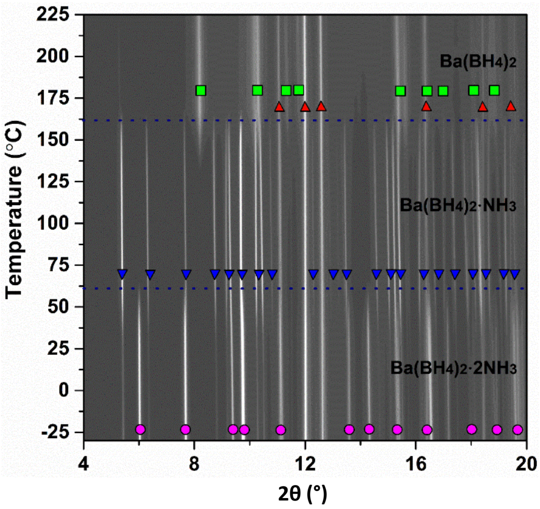

Figure 6. In situ SR-PXD for sample **s2** measured from −30 to 225 °C ($\Delta T/\Delta t$ = 5 °C/min, p(Ar) = 1 bar, λ = 0.7129 Å). $Ba(BH_4)_2 \cdot 2NH_3$ (pink circles), $Ba(BH_4)_2 \cdot NH_3$ (blue triangles), $Ba(BH_4)_2$ (green squares), BaH_2 (red triangles).

2.4. Thermal Analysis

Thermal analysis, including thermogravimetry, differential scanning calorimetry and mass spectrometry (TGA-DSC-MS), of sample **s2** suggests that ammonia is released in two steps, similar to the in situ SR-PXD, see Figure 7. The release of ammonia is initiated prior to the measurement, confirming the low thermal stability of $Ba(BH_4)_2{\cdot}2NH_3$. A release of 2.2 wt % of NH_3 is observed in the temperature range of 30 to 55 °C, which is lower than expected for one NH_3 equivalent, both due to the partial release prior to the measurement, and the mixture of $Ba(BH_4)_2{\cdot}2NH_3$, $Ba(BH_4)_2{\cdot}NH_3$ and BaH_2 in the as-synthesized sample. In the temperature range of 80 to 122 °C, a second mass loss of 6.4 wt % is observed, corresponding to the release of one NH_3 equivalent from $Ba(BH_4)_2{\cdot}NH_3$ to form $Ba(BH_4)_2$. The calculated mass loss according to the composition of sample **s2** is 5.2 wt % in the first step and 6.7 wt % in the second step. The differences between the calculated and observed mass losses are attributed to the partial NH_3 release prior to the measurement. The decomposition pathway is in agreement with the in situ SR-PXD data and Equation (2), but the temperatures for NH_3 release are significantly lower in the TGA-DSC-MS measurement. This is due to the close correlation between the thermal stability and the partial pressure of NH_3, which is also observed for other ammine metal borohydrides, e.g., $M(BH_4)_2{\cdot}xNH_3$ ($M = Ca^{2+}$ and Sr^{2+}) [25]. This is also observed for $RE(BH_4)_3{\cdot}xNH_3$ ($RE = La^{3+}$, Ce^{3+}), where in situ SR-PXD was performed in closed capillaries and in dynamic vacuum, respectively, changing the ammonia desorption temperatures by up to 75 °C [26].

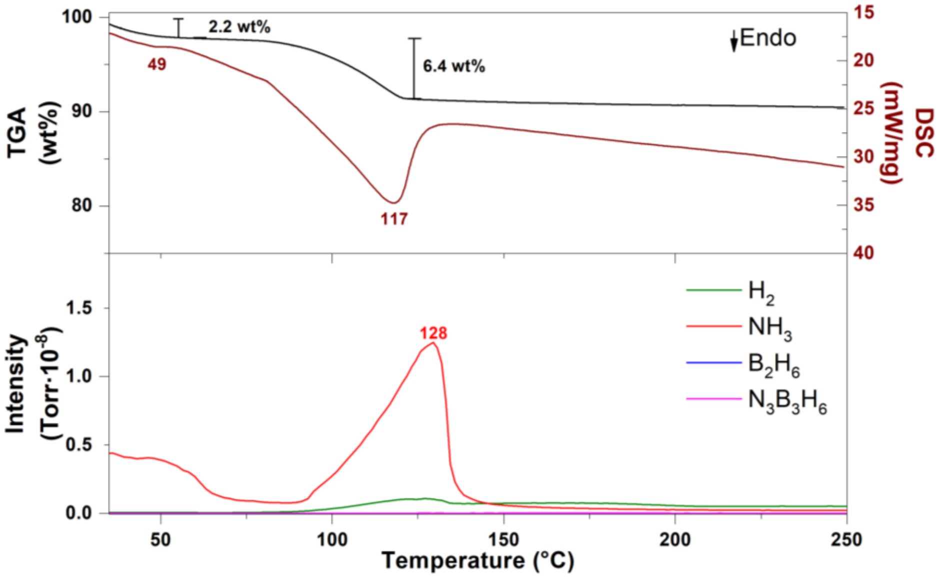

Figure 7. (**Top**) TGA/DSC for sample **s2** during heating from 30 to 250 °C ($\Delta T/\Delta t$ = 5 °C/min, 40 mL/min argon flow). (**Bottom**) Corresponding MS signals.

2.5. Mechanism for Thermal Decomposition

$M(BH_4)_2{\cdot}xNH_3$ ($M = Ca^{2+}$, Sr^{2+}, Ba^{2+} and $x = 1, 2$) decompose via the release of ammonia, reforming the metal borohydride. In contrast, $Mg(BH_4)_2{\cdot}xNH_3$ ($x = 1, 2$) release H_2 during decomposition, due to the higher charge density of Mg^{2+} [19,25,44]. Considering the similar decomposition pathway for $M = Ca^{2+}$, Sr^{2+} and Ba^{2+}, an increasing ionic radius down the group should result in lower decomposition temperatures, due to a lower charge density on the metal cation, and a correspondingly weaker M–N bond. This correlation is illustrated in Figure 8, and a linear correlation between the decomposition temperatures and ionic radii of the metal cations is observed for $M(BH_4)_2{\cdot}NH_3$. A similar trend is expected for $M(BH_4)_2{\cdot}2NH_3$, but $Sr(BH_4)_2{\cdot}2NH_3$ exhibits a similar thermal stability as $Ca(BH_4)_2{\cdot}2NH_3$, while $Ba(BH_4)_2{\cdot}2NH_3$ is significantly less stable.

This demonstrates that the charge density alone cannot explain the thermal stability, and it is also influenced by other parameters, e.g., the crystal structure.

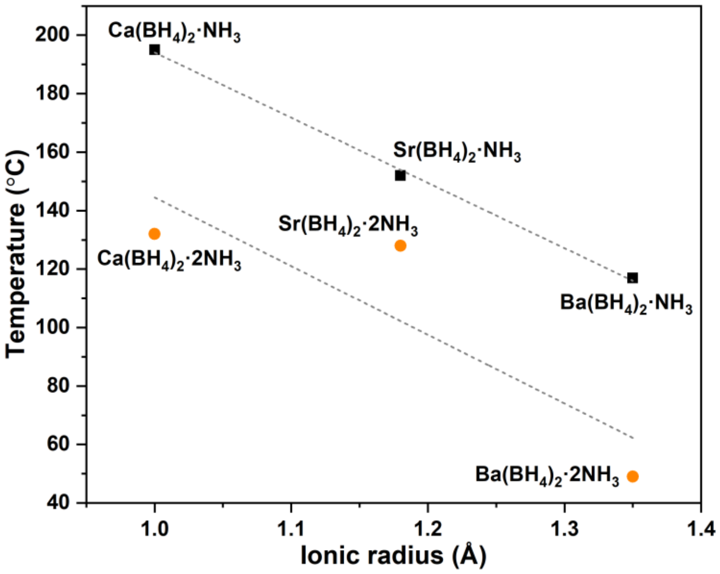

Figure 8. Decomposition temperatures for $M(BH_4)_2{\cdot}xNH_3$ (M = Ca^{2+}, Sr^{2+}, Ba^{2+} and x = 1, 2) [25]. The black squares and orange circles show the decomposition temperatures (maxima of the differential scanning calorimetry (DSC) signal) of $M(BH_4)_2{\cdot}NH_3$ and $M(BH_4)_2{\cdot}2NH_3$, respectively. The dashed lines show the correlation between decomposition temperatures and the ionic radii of the metal cations.

3. Materials and Methods

3.1. Sample Preparation

Barium borohydride, $Ba(BH_4)_2$ (**s1**), was synthesized using a modification of a recently published solvent-based approach [45]. Ba metal was hydrogenated by heating to T = 400 °C with a heating rate of $\Delta T/\Delta t$ = 5 °C/min in a hydrogen atmosphere, $p(H_2)$ = 140 bar. The resulting BaH_2 was ball milled in order to decrease the particle size and enhance the reactivity. For ball milling, a Fritsch Pulverisette 6 was used. The powder was packed in an argon atmosphere in an 80 mL tungsten carbide vial together with four tungsten carbide balls (diameter 10 mm) per gram of BaH_2. The powders were ball milled at 350 RPM for 10 min, followed by a 2 min break. This sequence was repeated 10 times (100 min of total ball milling time). The ball-milled BaH_2 was added to a 100 mL reaction flask with a valve outlet. DMS-BH_3 (10 M in toluene, Sigma-Aldrich, St. Louis, MO, USA) was added to the powder in a molar ratio of 3:1 (50% excess of DMS-BH_3), and diluted to a 5 M solution by adding toluene (anhydrous, Sigma-Aldrich). The reaction mixture was left to stir at 45 °C for a week. The powder was dried at 45 °C using a dynamic vacuum to remove any solvents present. A white powder was isolated.

Sample **s2** was prepared by a reaction between $Ba(BH_4)_2$ (**s1**) and dry NH_3-gas. $Ba(BH_4)_2$ was added to an argon-filled 100 mL flask with a valve outlet and a septum. The reaction flask was cooled to T = −10 °C using an ice–saltwater bath and NH_3 gas was added slowly while stirring and using a balloon to account for the pressure increase. After 1 h of NH_3 exposure, a dynamic vacuum was applied for five minutes at T = −10 °C to remove any excess gas. No color change was detected during the synthesis.

All sample handling and preparation was performed in an inert argon atmosphere using a glovebox with a circulation purifier, $p(O_2, H_2O)$ below 1 ppm.

3.2. Synchrotron Radiation Powder X-ray Diffraction

Time-resolved in situ synchrotron radiation powder X-ray diffraction (SR-PXD) data were obtained at the Swiss-Norwegian Beam Lines (SNBL) at the European Synchrotron Radiation Facility (ESRF) in Grenoble, France, with a Pilatus area detector, $\lambda = 0.7129$ Å [46]. The samples were packed in 0.5 mm borosilicate capillaries in a glovebox and sealed with grease. During measurement, the samples were heated from $T = -30$ °C to 225 °C with a heating rate of $\Delta T/\Delta t = 5$ °C/min using an Oxford Cryostream 700+. The samples were kept in the freezer prior to measurement. The X-ray exposure time was 10 s and the samples were rotated during the measurement.

3.3. Structural Solution and Refinement

The crystal structures were solved and refined from SR-PXD data. Indexing of the unit cell was performed in the program FOX, using the method of "decomposition-aided indexing" [30,47]. From careful inspection of systematic absences, the space group was determined. The powder X-ray diffraction pattern was compared to possible isostructural compounds and $Ba(BH_4)_2{\cdot}2NH_3$ was found to be isostructural to $Sr(BH_4)_2{\cdot}2NH_3$, as confirmed by subsequent Rietveld refinement. The structure of $Ba(BH_4)_2{\cdot}NH_3$ was solved at $T = 95$ °C by ab initio structure solution by global optimization in direct space, as implemented in FOX. The structural models were refined by the Rietveld method in the program Fullprof, and were checked for higher symmetry using the ADDSYM procedure implemented in Platon [48,49].

During Rietveld refinement, the background was described by linear interpolation between selected points, while pseudo-Voigt profile functions were used to fit the diffraction peaks. Generally, scale factor, unit cell parameters, zero-shift, profile parameters and temperature factors B were refined. For new structures, the atomic positions were also refined. NH_3 and BH_4^- were treated as rigid bodies during structure solution and Rietveld refinement.

3.4. Fourier Transform Infrared Spectroscopy

Sample **s1** and **s2** were characterized by infrared absorption spectroscopy using a NICOLET 380 FT-IR from Thermo Electron Corporation (Waltham, MA, USA), while an IRSpirit from Shimadzu (Kyoto, Japan) was used for BaH_2. The samples were measured in the scanning range 500–4000 cm^{-1} with 32 scans and a spectral resolution of 4 cm^{-1}. The 32 scans were averaged. Samples **s1** and **s2** were exposed to air for approximately 20 s during measurement, while BaH_2 was measured in an argon atmosphere.

3.5. Thermal Analysis and Mass Spectroscopy

Thermogravimetric analysis (TGA) and differential scanning calorimetry (DSC) were measured using a STA 6000 from PerkinElmer (Waltham, MA, USA) coupled with a mass spectrometer (MS), HPR-20 QMS sampling system from Hiden Analytical (Warrington, UK). Approximately 5 mg of sample were placed in a Al_2O_3 crucible and heated from 30 to 250 °C with a heating rate of $\Delta T/\Delta t = 5$ °C/min and an argon flow of 40 mL/min. The outlet gases were detected for hydrogen ($m/z = 2$), ammonia ($m/z = 17$), diborane ($m/z = 27$) and borazine ($m/z = 80$) using mass spectrometry.

4. Conclusions

Synthesis, characterization and structure determination were carried out for the ammine barium borohydrides, $Ba(BH_4)_2{\cdot}xNH_3$ ($x = 1, 2$). $Ba(BH_4)_2{\cdot}2NH_3$ crystallizes in an orthorhombic unit cell with space group symmetry $Pnc2$, where Ba^{2+} is octahedrally coordinated to four bridging BH_4^- groups and two NH_3 groups, forming a two-dimensional layered structure, isostructural to $Sr(BH_4)_2{\cdot}2NH_3$. A new structure type is observed for $Ba(BH_4)_2{\cdot}NH_3$, which crystallizes in an orthorhombic unit cell with space group symmetry $P2_12_12_1$. Ba^{2+} is coordinated by one NH_3 molecule and six bridging BH_4^- groups in a square-face monocapped trigonal prismatic geometry, where the prisms are connected to form distorted hexagonal six-fold chains in the *bc* plane, which run along the *a*-axis. $Ba(BH_4)_2{\cdot}xNH_3$ ($x = 1, 2$) decompose upon heating via the release of ammonia, similar to $M(BH_4)_2{\cdot}xNH_3$ ($M = Ca^{2+}$, Sr^{2+}). $Ba(BH_4)_2{\cdot}2NH_3$ is unstable at room temperature, and gradually releases NH_3, while it is fully decomposed to $Ba(BH_4)_2{\cdot}NH_3$ at 55 °C. $Ba(BH_4)_2{\cdot}NH_3$ fully decomposes to $Ba(BH_4)_2$ at 122 °C. The thermal stability is higher when measured by in situ SR-PXD performed in closed capillaries, due to the higher partial pressure of ammonia, which stabilizes the compounds. The decomposition temperature of the ammine alkaline earth metal (Ca, Sr and Ba) borohydrides decreases down the group due to the decreasing ionic radii of the metal cations. $Sr(BH_4)_2{\cdot}2NH_3$ is significantly more stable than suggested by this simple relation, suggesting that other factors influence the thermal stability and that the ionic potential of the metal cation should be calculated to provide further insight.

Supplementary Materials: The following are available online at http://www.mdpi.com/2304-6740/8/10/57/s1, crystallographic information files (CIF) are available as CCDC 2026487–2026488. These data can be obtained free of charge via www.ccdc.cam.ac.uk/data_request/cif, by emailing data_request@ccdc.cam.ac.uk, or by contacting The Cambridge Crystallographic Data Centre, 12 Union Road, Cambridge CB2 1EZ, UK; fax: +44 1223 336033.

Author Contributions: Conceptualization, J.B.G. and T.R.J.; formal analysis, J.B.G. and M.B.A.; investigation, J.B.G. and M.B.A.; writing—original draft preparation, J.B.G. and M.B.A.; writing—review and editing, J.B.G., M.B.A. and T.R.J.; supervision and project administration, T.R.J.; funding acquisition, T.R.J.; All authors have read and agreed to the published version of the manuscript.

Funding: The work was supported by the Danish Council for Independent Research, Technology and Production (HyNanoBorN, 4181-00462 and SOS-MagBat, 9041-00226B), Nordforsk via the project Functional Hydrides—FunHy (no. 81942), CarlsbergFondet, the Danish Natural Science Research Councils (DanScatt) and the SMART research initiative, an ESS Research Environment, where funding from the Danish Ministry of Higher Education and Science (UFM) is gratefully acknowledged.

Acknowledgments: We acknowledge the Swiss-Norwegian beamline BM01 at ESRF and the local contact Iurii Dovgaliuk for assistance with data collection. Affiliation with the Center for Integrated Materials Research (iMAT) at Aarhus University is gratefully acknowledged.

Conflicts of Interest: The authors declare no conflict of interest.

References

1. Paskevicius, M.; Jepsen, L.H.; Schouwink, P.; Černý, R.; Ravnsbæk, D.B.; Filinchuk, Y.; Dornheim, M.; Besenbacher, F.; Jensen, T.R. Metal borohydrides and derivatives—Synthesis, structure and properties. *Chem. Soc. Rev.* **2017**, *46*, 1565–1634. [CrossRef] [PubMed]
2. Møller, K.T.; Sheppard, D.; Ravnsbæk, D.B.; Buckley, C.E.; Akiba, E.; Li, H.W.; Jensen, T.R. Complex metal hydrides for hydrogen, thermal and electrochemical energy storage. *Energies* **2017**, *10*, 1645. [CrossRef]
3. Hirscher, M.; Yartys, V.A.; Baricco, M.; Bellosta von Colbe, J.; Blanchard, D.; Bowman, R.C.; Broom, D.P.; Buckley, C.E.; Chang, F.; Chen, P.; et al. Materials for hydrogen-based energy storage—Past, recent progress and future outlook. *J. Alloys Compd.* **2020**, *827*, 153548. [CrossRef]
4. Hadjixenophontos, E.; Dematteis, E.M.; Berti, N.; Wołczyk, A.R.; Huen, P.; Brighi, M.; Le, T.T.; Santoru, A.; Payandeh, S.; Peru, F.; et al. A Review of the MSCA ITN ECOSTORE—Novel Complex Metal Hydrides for Efficient and Compact Storage of Renewable Energy as Hydrogen and Electricity. *Inorganics* **2020**, *8*, 17. [CrossRef]
5. Hagemann, H. Boron hydrogen compounds for hydrogen storage and as solid ionic conductors. *Chimia* **2019**, *73*, 868–873. [CrossRef]
6. Schouwink, P.; Didelot, E.; Lee, Y.S.; Mazet, T.; Černý, R. Structural and magnetocaloric properties of novel gadolinium borohydrides. *J. Alloys Compd.* **2016**, *664*, 378–384. [CrossRef]
7. Grinderslev, J.B.; Møller, K.T.; Bremholm, M.; Jensen, T.R. Trends in Synthesis, Crystal Structure, and Thermal and Magnetic Properties of Rare-Earth Metal Borohydrides. *Inorg. Chem.* **2019**, *58*, 5503–5517. [CrossRef]
8. Wegner, W.; van Leusen, J.; Majewski, J.; Grochala, W.; Kögerler, P. Borohydride as Magnetic Superexchange Pathway in Late Lanthanide Borohydrides. *Eur. J. Inorg. Chem.* **2019**, *2019*, 1776–1783. [CrossRef]
9. Marks, S.; Heck, J.G.; Habicht, M.H.; Oña-Burgos, P.; Feldmann, C.; Roesky, P.W. $[Ln(BH_4)_2(THF)_2]$ (Ln = Eu, Yb)—A highly luminescent material. Synthesis, properties, reactivity, and NMR studies. *J. Am. Chem. Soc.* **2012**, *134*, 16983–16986. [CrossRef]

10. Schouwink, P.; Ley, M.B.; Tissot, A.; Hagemann, H.; Jensen, T.R.; Smrčok, L'.; Černý, R. Structure and properties of complex hydride perovskite materials. *Nat. Commun.* **2014**, *5*, 1–10. [CrossRef]
11. Ley, M.B.; Ravnsbæk, D.B.; Filinchuk, Y.; Lee, Y.S.; Janot, R.; Cho, Y.W.; Skibsted, J.; Jensen, T.R. LiCe$(BH_4)_3$Cl, a new lithium-ion conductor and hydrogen storage material with isolated tetranuclear anionic clusters. *Chem. Mater.* **2012**, *24*, 1654–1663. [CrossRef]
12. de Jongh, P.E.; Blanchard, D.; Matsuo, M.; Udovic, T.J.; Orimo, S. Complex hydrides as room-temperature solid electrolytes for rechargeable batteries. *Appl. Phys. A Mater. Sci. Process.* **2016**, *122*, 1–6. [CrossRef]
13. Matsuo, M.; Nakamori, Y.; Orimo, S.I.; Maekawa, H.; Takamura, H. Lithium superionic conduction in lithium borohydride accompanied by structural transition. *Appl. Phys. Lett.* **2007**, *91*, 224103. [CrossRef]
14. Mohtadi, R.; Matsui, M.; Arthur, T.S.; Hwang, S.J. Magnesium borohydride: From hydrogen storage to magnesium battery. *Angew. Chem. Int. Ed.* **2012**, *51*, 9780–9783. [CrossRef] [PubMed]
15. Heere, M.; Hansen, A.L.; Payandeh, S.H.; Aslan, N.; Gizer, G.; Sørby, M.H.; Hauback, B.C.; Pistidda, C.; Dornheim, M.; Lohstroh, W. Dynamics of porous and amorphous magnesium borohydride to understand solid state Mg-ion-conductors. *Sci. Rep.* **2020**, *10*, 1–11. [CrossRef] [PubMed]
16. Makepeace, J.W.; He, T.; Weidenthaler, C.; Jensen, T.R.; Chang, F.; Vegge, T.; Ngene, P.; Kojima, Y.; de Jongh, P.E.; Chen, P.; et al. Reversible ammonia-based and liquid organic hydrogen carriers for high-density hydrogen storage: Recent progress. *Int. J. Hydrogen Energy* **2019**, *44*, 7746–7767. [CrossRef]
17. Jepsen, L.H.; Ley, M.B.; Lee, Y.S.; Cho, Y.W.; Dornheim, M.; Jensen, J.O.; Filinchuk, Y.; Jørgensen, J.E.; Besenbacher, F.; Jensen, T.R. Boron-nitrogen based hydrides and reactive composites for hydrogen storage. *Mater. Today* **2014**, *17*, 129–135. [CrossRef]
18. Jepsen, L.H.; Ley, M.B.; Černý, R.; Lee, Y.S.; Cho, Y.W.; Ravnsbæk, D.; Besenbacher, F.; Skibsted, J.; Jensen, T.R. Trends in Syntheses, Structures, and Properties for Three Series of Ammine Rare-Earth Metal Borohydrides, $M(BH_4)_3 \cdot nNH_3$ (M = Y, Gd, and Dy). *Inorg. Chem.* **2015**, *54*, 7402–7414. [CrossRef]
19. Soloveichik, G.; Her, J.H.; Stephens, P.W.; Gao, Y.; Rijssenbeek, J.; Andrus, M.; Zhao, J.C. Ammine magnesium borohydride complex as a new material for hydrogen storage: Structure and properties of $Mg(BH_4)_2 \cdot 2NH_3$. *Inorg. Chem.* **2008**, *47*, 4290–4298. [CrossRef]
20. Filippov, S.; Grinderslev, J.B.; Andersson, M.S.; Armstrong, J.; Karlsson, M.; Jensen, T.R.; Klarbring, J.; Simak, S.I.; Häussermann, U. Analysis of Dihydrogen Bonding in Ammonium Borohydride. *J. Phys. Chem. C* **2019**, *123*, 28631–28639. [CrossRef]
21. Grinderslev, J.B.; Jepsen, L.H.; Lee, Y.-S.; Møller, K.T.; Cho, Y.W.; Cerny, R.; Jensen, T.R. Structural Diversity and Trends in Properties of an Array of Hydrogen-Rich Ammonium Metal Borohydrides. *Inorg. Chem.* **2020**, *59*, 12733–12747. [CrossRef] [PubMed]
22. Yan, Y.; Grinderslev, J.B.; Lee, Y.-S.; Jørgensen, M.; Cho, Y.W.; Černý, R.; Jensen, T.R. Ammonia-assisted fast Li-ion conductivity in a new hemiammine lithium borohydride, $LiBH_4 \cdot ½NH_3$. *Chem. Commun.* **2020**, *56*, 3971–3974. [CrossRef] [PubMed]
23. Yan, Y.; Dononelli, W.; Jørgensen, M.; Grinderslev, J.B.; Lee, Y.-S.; Cho, Y.W.; Černý, R.; Hammer, B.; Jensen, T.R. The mechanism of Mg^{2+} conduction in ammine magnesium borohydride promoted by a neutral molecule. *Phys. Chem. Chem. Phys.* **2020**, *22*, 9204–9209. [CrossRef] [PubMed]
24. Yan, Y.; Grinderslev, J.B.; Jørgensen, M.; Skov, L.N.; Skibsted, J.; Jensen, T.R. Ammine Magnesium Borohydride Nanocomposites for All-Solid-State Magnesium Batteries. *ACS Appl. Energy Mater.* **2020**, *3*, 9264–9270. [CrossRef]
25. Jepsen, L.H.; Lee, Y.S.; Černý, R.; Sarusie, R.S.; Cho, Y.W.; Besenbacher, F.; Jensen, T.R. Ammine Calcium and Strontium Borohydrides: Syntheses, Structures, and Properties. *ChemSusChem* **2015**, *8*, 3472–3482. [CrossRef] [PubMed]
26. Grinderslev, J.B.; Ley, M.B.; Lee, Y.-S.; Jepsen, L.H.; Jørgensen, M.; Cho, Y.W.; Skibsted, J.; Jensen, T.R. Ammine Lanthanum and Cerium Borohydrides, $M(BH_4)_3 \cdot nNH_3$; Trends in Synthesis, Structures, and Thermal Properties. *Inorg. Chem.* **2020**, *59*, 7768–7778. [CrossRef]
27. Richter, B.; Ravnsbæk, D.B.; Tumanov, N.; Filinchuk, Y.; Jensen, T.R. Manganese borohydride; Synthesis and characterization. *Dalt. Trans.* **2015**, *44*, 3988–3996. [CrossRef]
28. Yan, Y.; Li, H.W.; Sato, T.; Umeda, N.; Miwa, K.; Towata, S.; Orimo, S. Dehydriding and rehydriding properties of yttrium borohydride $Y(BH_4)_3$ prepared by liquid-phase synthesis. *Int. J. Hydrogen Energy* **2009**, *34*, 5732–5736. [CrossRef]

29. Rude, L.H.; Corno, M.; Ugliengo, P.; Baricco, M.; Lee, Y.S.; Cho, Y.W.; Besenbacher, F.; Overgaard, J.; Jensen, T.R. Synthesis and structural investigation of $Zr(BH_4)_4$. *J. Phys. Chem. C* **2012**, *116*, 20239–20245. [CrossRef]
30. Ravnsbœk, D.B.; Sørensen, L.H.; Filinchuk, Y.; Besenbacher, F.; Jensen, T.R. Screening of metal borohydrides by mechanochemistry and diffraction. *Angew. Chem. Int. Ed.* **2012**, *51*, 3582–3586. [CrossRef]
31. Li, S.; Yang, B.; Tang, S.; Lai, T.; Xiang, J.; Wang, L. Chemical synthesis and characterization of zinc borohydride. *Procedia Eng.* **2012**, *27*, 1420–1425. [CrossRef]
32. Roedern, E.; Jensen, T.R. Ammine-Stabilized Transition-Metal Borohydrides of Iron, Cobalt, and Chromium: Synthesis and Characterization. *Inorg. Chem.* **2015**, *54*, 10477–10482. [CrossRef] [PubMed]
33. Jepsen, L.H.; Ley, M.B.; Filinchuk, Y.; Besenbacher, F.; Jensen, T.R. Tailoring the Properties of Ammine Metal Borohydrides for Solid-State Hydrogen Storage. *ChemSusChem* **2015**, *8*, 1452–1463. [CrossRef] [PubMed]
34. Huang, J.; Tan, Y.; Su, J.; Gu, Q.; Černý, R.; Ouyang, L.; Sun, D.; Yu, X.; Zhu, M. Synthesis, structure and dehydrogenation of zirconium borohydride octaammoniate. *Chem. Commun.* **2015**, *51*, 2794–2797. [CrossRef]
35. Yuan, F.; Chen, X.; Gu, Q.; Tang, Z.; Yu, X. Synthesis of ammine dual-metal (V, Mg) borohydrides with enhanced dehydrogenation properties. *Int. J. Hydrogen Energy* **2013**, *38*, 5322–5329. [CrossRef]
36. Yuan, F.; Gu, Q.; Chen, X.; Tan, Y.; Guo, Y.; Yu, X. Complex ammine titanium(III) borohydrides as advanced solid hydrogen-storage materials with favorable dehydrogenation properties. *Chem. Mater.* **2012**, *24*, 3370–3379. [CrossRef]
37. Welchman, E.; Thonhauser, T. Decomposition mechanisms in metal borohydrides and their ammoniates. *J. Mater. Chem. A* **2017**, *5*, 4084–4092. [CrossRef]
38. Marynick, D.S.; Lipscomb, W.N. Crystal Structure of Beryllium Borohydride. *Inorg. Chem.* **1972**, *11*, 820–823. [CrossRef]
39. Sharma, M.; Didelot, E.; Spyratou, A.; Max Lawson Daku, L.; Černý, R.; Hagemann, H. Halide Free $M(BH_4)_2$ (M = Sr, Ba, and Eu) Synthesis, Structure, and Decomposition. *Inorg. Chem.* **2016**, *55*, 7090–7097. [CrossRef]
40. D'Anna, V.; Spyratou, A.; Sharma, M.; Hagemann, H. FT-IR spectra of inorganic borohydrides. *Spectrochim. Acta Part A Mol. Biomol. Spectrosc.* **2014**, *128*, 902–906. [CrossRef]
41. Olovsson, I.; Templeton, D.H. X-ray study of solid ammonia. *Acta Cryst.* **1959**, *12*, 832–836. [CrossRef]
42. Shannon, R.D. Revised effective ionic radii and systematic studies of interatomic distances in halides and chalcogenides. *Acta Cryst. Sect. A* **1976**, *32*, 751–767. [CrossRef]
43. Tang, Z.; Tan, Y.; Gu, Q.; Yu, X. A novel aided-cation strategy to advance the dehydrogenation of calcium borohydride monoammoniate. *J. Mater. Chem.* **2012**, *22*, 5312–5318. [CrossRef]
44. Yang, Y.; Liu, Y.; Li, Y.; Gao, M.; Pan, H. Synthesis and thermal decomposition behaviors of magnesium borohydride ammoniates with controllable composition as hydrogen storage materials. *Chem. Asian J.* **2013**, *8*, 476–481. [CrossRef]
45. Richter, B.; Grinderslev, J.B.; Møller, K.T.; Paskevicius, M.; Jensen, T.R. From Metal Hydrides to Metal Borohydrides. *Inorg. Chem.* **2018**, *57*, 10768–10780. [CrossRef] [PubMed]
46. Dyadkin, V.; Pattison, P.; Dmitriev, V.; Chernyshov, D. A new multipurpose diffractometer PILATUS@SNBL. *J. Synchrotron Radiat.* **2016**, *23*, 825–829. [CrossRef] [PubMed]
47. Favre-Nicolin, V.; Černý, R. FOX, "free objects for crystallography": A modular approach to ab initio structure determination from powder diffraction. *J. Appl. Cryst.* **2002**, *35*, 734–743. [CrossRef]
48. Rodriguez-Carvajal, R.J. *FULLPROF: A Program for Rietveld Refinement and Pattern Matching Analysis*; Abstracts of the Satellite Meeting on Powder Diffraction of the XV Congress of the IUCr; International Union of Crystallography: Toulouse, France, 1990; p. 127.
49. Spek, A.L. Structure validation in chemical crystallography. *Acta Cryst. Sect. D Biol. Cryst.* **2009**, *65*, 148–155. [CrossRef]